frontiers | Frontiers in Materials

TYPE Original Research
PUBLISHED 17 October 2022
DOI 10.3389/fmats.2022.1015112

OPEN ACCESS

EDITED BY
Evelyn KF Yim,
University of Waterloo, Canada

REVIEWED BY
Krishnamurithy Genasan,
University of Malaya, Malaysia
Ren-Jei Chung,
National Taipei University of Technology, Taiwan

*CORRESPONDENCE
Biao Chen,
chenbiao19701107@sina.com

SPECIALTY SECTION
This article was submitted to Biomaterials, a section of the journal Frontiers in Materials

RECEIVED 09 August 2022
ACCEPTED 26 September 2022
PUBLISHED 17 October 2022

CITATION
Zhou A, Chen S, Mickymaray S, Alqurashi YE, Jeraud M, Chen B and Hu Y (2022), Hydroxyapatite-collagen-carboxylic carbon quantum dot composite loaded with chrysin supported the proliferation and differentiation of human bone marrow derived mesenchymal stem cells. *Front. Mater.* 9:1015112. doi: 10.3389/fmats.2022.1015112

Hydroxyapatite-collagen-carboxylic carbon quantum dot composite loaded with chrysin supported the proliferation and differentiation of human bone marrow derived mesenchymal stem cells

Ao Zhou[1], Sinan Chen[2], Suresh Mickymaray[3], Yaser E. Alqurashi[3], Mathew Jeraud[4], Biao Chen[1]* and Yunjiu Hu[5]

[1]Department of Bone and Soft Tissue Oncology, Affiliated Cancer Hospital of Chongqing University, Chongqing, China, [2]Department of Orthopedics, The Second Affiliated Hospital of Chongqing Medical University, Chongqing, China, [3]Department of Biology, College of Science Al-zulfi, Majmaah University, Al-Majmaah, Saudi Arabia, [4]Ibn Sina National College for Medical Studies, Jeddah, Saudi Arabia, [5]Department of Emergency and Critical Care Medicine, The First Affiliated Hospital of Chongqing Medical University, Chongqing, China

Developing a bioactive scaffold with biocompatible material is a substantial approach to bone regeneration and functional healing. Hydroxyapatite (HAP) is the main component in bone formation as an inorganic component and regeneration due to its osteoconductive properties. In this study, we prepared a scaffold material composed of HAP and collagen (COL) cross-linked *via* carboxylic carbon quantum dots (CCQD) with a chrysin (CRN) molecule. CRN is a flavonoid that has been shown to encourage the bone development of bone marrow-derived mesenchymal stem cells. It is loaded for enhancing bone regeneration and HAP's growth ability. XRD, FT-IR, SEM, and TEM analysis have characterized the prepared composites for their crystalline nature, functional behavior, and morphological evaluations. The HAP has retained its original crystalline lattice confirmed from XRD analysis in the prepared composites. The addition of CRN molecule has decreased the length of HAP rods from ~932 nm to ~459 nm, as confirmed by TEM images. The increased particle sizes have been observed for the prepared composites. It reaches the maximum at 938.0 nm for the final HAP/COL/CCQD/CRN composite, which was confirmed by particle size analysis. The *in-vitro* CRN release behavior shows that the CRN molecule has controlled release up to 23% for 48 h. The biocompatibility of prepared material was investigated and confirmed on human bone marrow-derived mesenchymal stem cells (hBMSCs). This examination has proven that the prepared material is good for bone cell regeneration. The material may apply for bone regeneration applications after *in-vivo* and clinical investigations.

KEYWORDS

carbon quantum dot, collagen, flavonoid, hydroxyapatite, human bone marrow mesenchymal stem cells

1 Introduction

Bone injuries from the damage of bone are initiated by various bone diseases like osteoporosis, osteoarthritis, osteosarcoma, and different inflammatory processes that characterize a substantial problem for people and the healthcare systems. The three factors, such as 1) the size of the defect, 2) the defect site's stability, and 3) the bone quality of the patient, mainly represent the self-healing ability of bone along with other factors such as age and diabetes (Levingstone et al., 2019). There are several strategies, including the use of metal, ceramic, polymer-based implants, and synthetic bone materials like hydroxyapatite (HAP), β-tricalcium phosphate (β-TCP), and calcium phosphate-based cement utilized to treat various bone injuries (Jeong et al., 2019; Kim et al., 2020). However, whereas these choices are utilized universally in the orthopedic field, they are not devoid of problems, the best known of which is an infection and comprises pain and poorer bone re-forming abilities (Kręcisz et al., 2006; David and Nixon, 2020). To avoid these limitations, utilizing the bone regeneration approach would be ideal.

In this study, hydroxyapatite (HAP) bone renewing material facilitates higher bone renewing ability and involves higher resorption (Bharati et al., 2005; Prabakaran et al., 2021; Song et al., 2021). In 2021, Fu et al. reviewed the HAP-based polyester composites for bone regeneration applications (Fu et al., 2021). In the same year, Shi et al. reviewed the HAP-based materials for bone regeneration. They covered the Ions doped HAP, HAP/polymeric composites, surface modified HAP, and their polymeric composition (Shi et al., 2021). Despite the advantage of HAP in the bone healing process, HAP has not enlarged its reputation in the orthopedic field due to its brittleness and poor molding ability (Ingole et al., 2021). To overcome this issue, we have enhanced the mechanical strength of the HAP with collagen (COL) protein. In the organic phase of bone, COL is the most significant constituent, a force-sensitive protein with a diameter of 80–100 nm (Kamakura et al., 2006; Fratzl and Weinkamer, 2007; Thorpe et al., 2010). Antoniac et al. prepared the HAP-COL-based composite for bone healing purposes (Antoniac et al., 2021). Using the lyophilization technique, they prepared the two composites, such as 10% COL- 90% HAP composite and 10% COL- 80% HAP- 10% Mg composite using the lyophilization technique. They concluded that the established composite materials, consisting of COL with interconnected pore structure and nano-HAP and Mg particles adherent to the type 1 collagen fibrils, are better to serve as bone substitutes supporting bone healing and regeneration (Antoniac et al., 2021).

Due to the presence of cadmium and heavy indium metals, the quantum dots (QDs) (semiconductor nanocrystals smaller than the Bohr radius with noteworthy optical and electrical properties) produces some toxicity in medical applications (Luo et al., 2013; Ghorghi et al., 2020). The good photostability, biocompatibility, cellular uptake, and low toxicity nature of carbon quantum dots (CQDs) are used to replace QDs in biological detection and imaging applications (Rafienia et al., 2018). Currently, CQDs are extensively utilized in biosensors, biological capturing, and drug delivery systems (Lim et al., 2015). In 2020, Ghorghi et al. developed the electrospun nanofibers composed of captopril (CP)-loaded PCL-CQDs. They concluded that the scaffold containing CQDs and CP significantly increased the MG-63 human osteoblast-like cells' proliferation and ALP activity *in-vitro* (Ghorghi et al., 2020).

Several foodstuffs, including mushrooms, honey, and plants such as passiflora, consist of a 5,7-dihydroxyflavone, one dietary bioactive flavone commonly named chrysin (CRN). CRN has anti-inflammatory, anti-cancer, anti-diabetic, antioxidant, hepatoprotective, and anti-microbial properties (Reddy Kasala et al., 2015). In addition, it blocks the creation of osteoclast cells, and through the extracellular signal-regulated kinase (ERK/MAPK) signaling pathway, it encourages osteoblast formation and osteogenic differentiation (Zeng et al., 2013). The canonical extracellular signal-regulated kinase (ERK) MAPKs have two isoforms, ERK1 (MAPK3) and ERK2 (MAPK1), both of which are highly expressed in osteoblast-lineage cells. ERK1 and ERK2 MAPKs are activated by MAP2K MEK1 (MAP2K1) and MEK2 (MAP2K2) through phosphorylation of activation loop residues Thr202/Tyr204 and Thr185/Tyr187, respectively. Moreover, Jung-Min Kim et al., 2019 have demonstrated that ERK activation in osteoprogenitors is required for osteoblast differentiation and bone formation *via* control of osteoblast master regulators, including RUNX2, ATF4, and β-catenin (Min Kim et al., 2019). In 2018, Menon et al. fabricated the chitosan (CS)/carboxymethyl cellulose (CMC)/nano HAP composite to incorporate CRN molecule in various concentrations. They evaluated that the release of CRN molecule from the scaffold promotes the proliferation of mouse mesenchymal stem cells (mMSCs) and differentiation into osteoblasts, which would be enhanced by chrysin due to the osteoblast differentiation transcription factor Runx2 down-regulation (Haritha Menon et al., 2018). In 2021, Prabakaran et al. developed the mineral substituted HAP/CRN composite loaded with garlic ginger paste extract and gentamycin anti-biotics. They proved the non-toxic nature of the CRN molecule in MG-63 cells *in-vitro* (Prabakaran and Rajan, 2021).

Based on these analyses, we have developed the HAP/COL/CCQDs composite loaded with CRN molecule. The above-mentioned previous studies highly recommend the promising

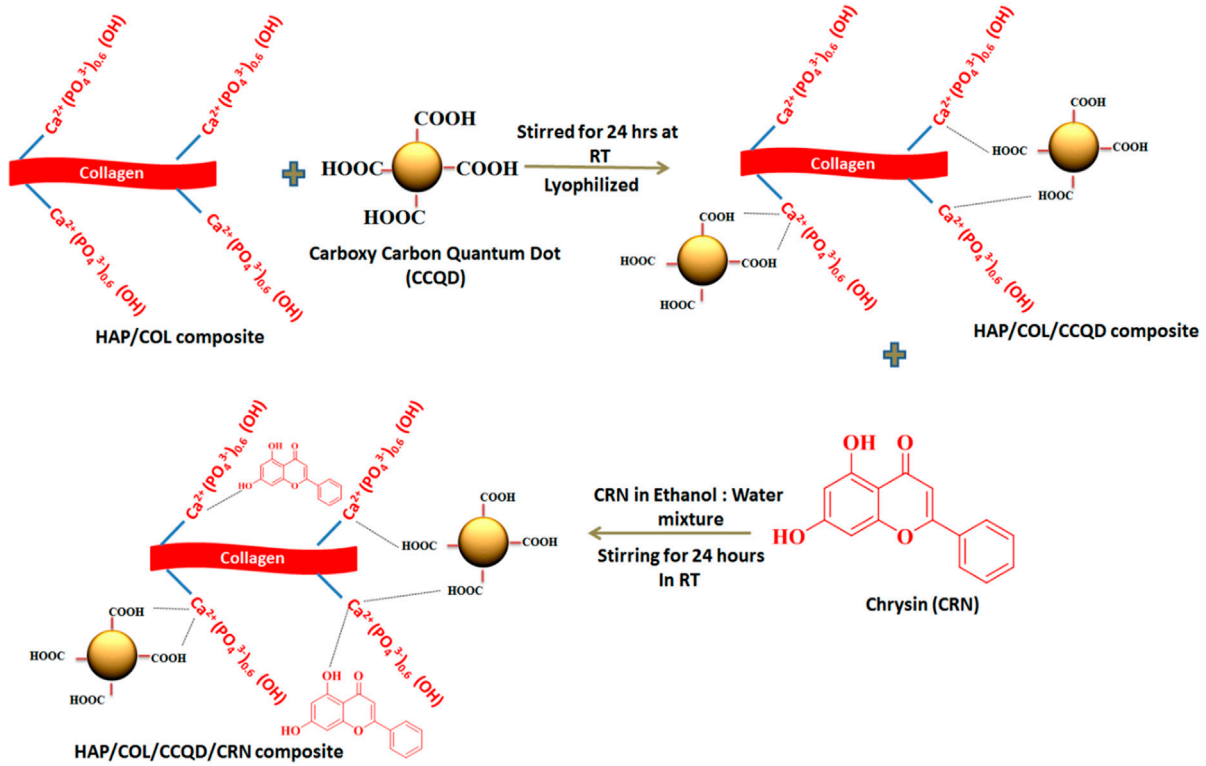

SCHEME 1
Mechanism of HAP/COL/CCQD/CRN composite formation. The CRN molecule is attached to the HAP/COL/CCQD composite *via* hydrogen bonding.

ability of these corresponding individual components to cure bone injuries without any infections. However, no elaborated studies are available to combine these components as composites. Thus, to enlarge the HAP/COL/CCQDs/CRN composite applications and promote their importance as a bone-regenerating material, we assessed the impact of this composite on the bone healing process.

2 Experimental section

2.1 Materials

All the chemicals required to prepare the desired bone regenerative composite were obtained from commercial sources and sued as such as received without further purification. Calcium Acetate Monohydrate $Ca(CH_3CO_2)_2.H_2O$, Citric Acid Anhydrous, and N-hydroxysuccinimide were purchased from SRL, India. Sodium Phosphate Monobasic Dihydrate $NaH_2PO_4.2H_2O$ was obtained from RANKEM, India. 1-(3-Dimethylaminopropyl)-3-ethyl carbodiimide hydrochloride (EDC) was received from CDH, India. Chrysin was purchased from Sigma-Aldrich, India. Double distilled water was used in the whole experiment.

2.2 Preparation of hydroxyapatite (HAP)

HAP was prepared from the direct precipitation method following the previous literature with slight modifications. Initially, 250 ml of 0.02M Ca and P solutions were separately prepared by dissolving the precursors $Ca(CH_3CO_2)_2.H_2O$ and $NaH_2PO_4.2H_2O$ in water, respectively. Then, the 250 ml of 0.02M Ca solution was slowly added to 250 ml of 0.02M $NaH_2PO_4.2H_2O$ solution for 1 h *via* burette. The mixture solution was stirred at 400 rpm at 65°C for 4 h under a magnetic stirrer. The formed white precipitate was filtered, then dried at 60°C in an oven and crushed with mortar to get the fine HAP particles. The pH of 5.5 was maintained throughout the reaction (Ma, 2019).

2.3 Preparation of HAP/COL composite

COL was dissolved in water and adjusted to 3% of the final pH of 7.4. HAP powder was mixed with 3% collagen, with 77% of the weight percentage of HAP in the HAP/COL composite. Then, the HAP/COL mixture was lyophilized at −40°C. The collected HAP/COL composite was then subjected to de hydrothermal treatment

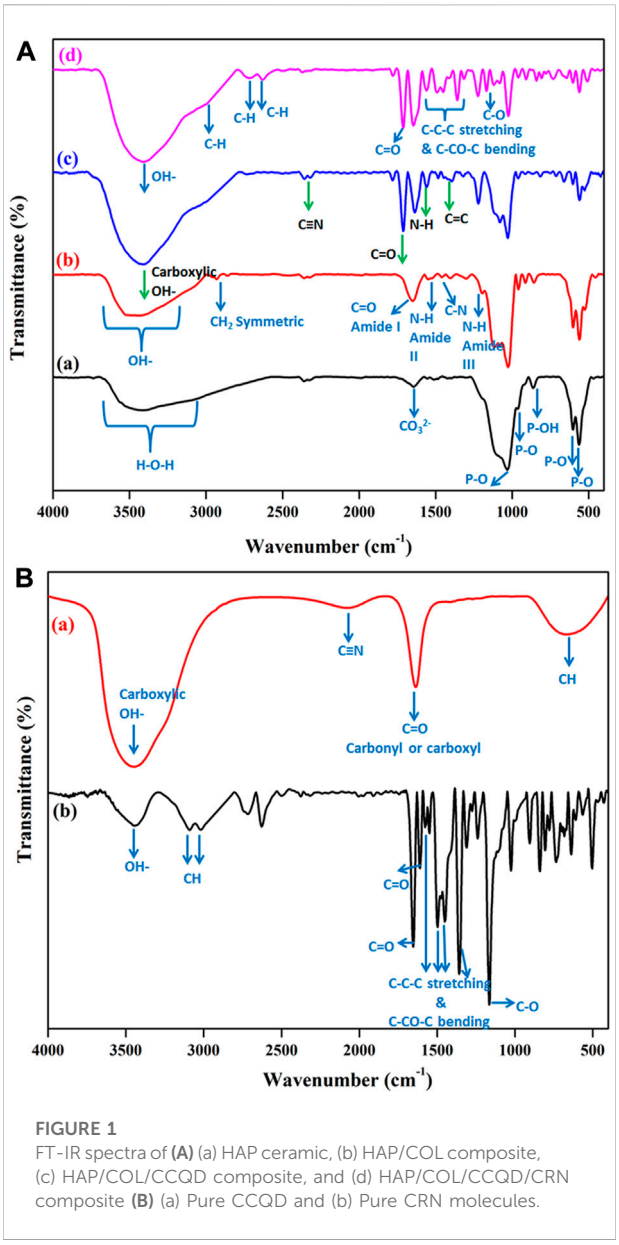

FIGURE 1
FT-IR spectra of **(A)** (a) HAP ceramic, (b) HAP/COL composite, (c) HAP/COL/CCQD composite, and (d) HAP/COL/CCQD/CRN composite **(B)** (a) Pure CCQD and (b) Pure CRN molecules.

under a hot air oven at 150°C for 24 h to get the pure form of HAP/COL composite (Kamakura et al., 2006; Kawai et al., 2009).

2.4 Preparation of carboxylic carbon quantum dot (CCQD)

By direct pyrolyzing of Citric acid (CA), a Carboxylic Carbon Quantum Dot (CCQD) was prepared. Shortly, 3 g CA was heated to 200°C in a furnace for 2 h. While heating the CA in the furnace, first, CA was undergone a liquefaction process. The color change of the CA liquid from colorless to orange indicates the materialization of CCQD. Then, the obtained CCQD sample was dialyzed in a 1,000 Da molecular weight dialysis bag in DD water for 3 days to get the pure form of the product. Finally, the products were lyophilized at −40°C and stored in a dryer until further use (Sun and Wu, 2018).

2.5 Preparation of HAP/COL/CCQD composite

At first, the CCQD (1.5 g) was needed to activate by using 100 mg EDC and 50 mg of NHS for 2 h. Then 100 mg of HAP/COL was added to this activated CCQD (60 mg) solution and stirred for 24 h under a magnetic stirrer at room temperature (RT). Then the reaction mixture was lyophilized and dried to get the HAP/COL/CCQD composite (Heydari et al., 2017).

2.6 Preparation of chrysin (CRN) loaded HAP/COL/CCQD composite

For the CRN-loaded HAP/COL/CCQD composite, the 20 mg of CRN was dissolved in water: ethanol mixture of a 1:0.5 ratio. Then, this solution was added to 100 mg of the above prepared HAP/COL/CCQD composite under stirring conditions for 24 h, and the final product was lyophilized at −40°C to get the pure product. The formation of the composite was given in Scheme 1.

2.7 Physicochemical characterizations

2.7.1 Fourier transform infra-red (FT-IR) analysis

The composite's and individual components' functional groups and their interactions with each other were evaluated by Fourier Transform Infra-Red (FT-IR) spectroscopy obtained from IRTRACER-100, Shimadzu. The spectra were acquired within the scanning range of 4,000–400 cm^{-1} after preparing the samples with a KBr pellet.

2.7.2 X-ray diffraction (XRD) analysis

X-ray diffraction (XRD) instrument (Bruker ECO D8 Advance model) was utilized to evaluate the phase characteristics and crystallinity of the prepared composites. The scanning process was performed by running the instrument with Cu anode at 40 kV and 25 mA scanning angle from 10° to 99° and scanning rate (2θ) of 10.

2.7.3 Scanning electron microscope (SEM) analysis

The surface morphology of the prepared composites was examined by the Scanning electron microscope (SEM) equipped with Energy Dispersive X-ray (EDX) (VEGA3 TESCAN). The samples were dispersed in water at 27°C, and it was coated on the glass plate, and then dried at RT for SEM scanning analysis.

TABLE 1 The forward and reverse sequences of the primers.

Gene	Forward primer sequences	Reverse primer sequences
Runx2	CCACCGAGACCAACAGAGTC	GTCACTGTGCTGAAGAGGCT
OCN	TGAGACCCTCACACTCCTC	ACCTTTGCTGGACTCTGCAC
VEGF	CGCTCGGTGCTGGAATTTG	AGGTAGAGCAGCAAGGCAAG

2.7.4 Transmission electron microscope (TEM) analysis

The microstructure of all prepared composites was investigated with High-Resolution Transmission Electron Microscope (HR-TEM) instrument (FEI Technai $G^2$20 S-TWIN TEM). The samples prepared for SEM analysis were also used to take TEM morphology by coating the dispersed samples on the Cu grid. ImageJ software (V 1.8.0) estimated the average diameter of the composites.

2.7.5 Particle size analysis

An instrument from Nanoplus Particulate systems was utilized for diameter distribution and cumulant particle size measurements. All the samples were dispersed in water and analyzed at 25°C.

2.7.6 Drug entrapment efficiency, loading capacity, and release analysis

To calculate the CRN drug entrapment efficiency and loading capacity from HAP/COL/CCQD/CRN composite. 20 mg of HAP/COL/CCQD/CRN composite were dissolved in 15 ml of ethanol solution and subjected to vortex for 30 min. Then, the solution obtained was centrifuged at 3,000 rpm for 15 min. The absorption intensity of CRN was measured using UV-vis spectroscopy at the λ_{max} value of 270 nm. The entrapment efficiency and loading capacity were calculated from the following Equations 1, 2, respectively.

$$\text{LC}\ (\%) = \frac{\text{Total amount of CRN} - \text{Free amount of CRN}}{\text{Weight of the dried composite}}\ \text{X}\ 100 \quad (1)$$

$$\text{EE}\ (\%) = \frac{\text{Total amount of CRN} - \text{Free amount of CRN}}{\text{Total amount of CRN}}\ \text{X}\ 100 \quad (2)$$

The CRN drug released from the HAP/COL/CCQD/CRN carrier (25 mg) at pH 7.4 for 50 h was calculated using the dialysis method in 50 ml of PBS solution under stirring conditions. At the predetermined time interval, 2 ml of the CRN-released PBS medium was replaced with a freshly prepared PBS solution. The concentration of CRN release was analyzed by UV-Vis spectroscopy at 270 nm. The release percentage was calculated from the following Equation 3.

$$\text{Release}\ (\%) = \frac{\text{Released CRN molecule}}{\text{Total loaded CRN molecule}}\ \text{X}\ 100 \quad (3)$$

2.8 Biological Characterizations

2.8.1 hBMSCs culture

hBMSCs were acquired from ATCC and cultivated in the knock-out medium (from Sigma) containing Fetal Bovine Serum (FBS -10%), fungicide (0.1%), antibiotics (100 μg/ml of streptomycin, and 100 U/mL of penicillin) and accompanied with fibroblast GF-basic (2 ng/ml) (bFGF-Peprotech, United States). Then the cultured cells were saved in a humidified incubator at 37°C under 5% CO_2 flow.

2.8.2 Cytocompatibility evaluation by MTT assay

MTT assay was utilized here to estimate the cell attachment and proliferation quantitatively. All the experimental samples were sterilized with 75% alcohol, followed by PBS washing three times and overnight soaking in DMEM/F12 (50/50) medium comprising FBS (10%) before cell seeding. hBMSCs were fixed as control cells in the absence of any composites. Then, hBMSCs were seeded in 24-well plates at a density of 1×10^4 cells per well for the cell attachment and proliferation assay. The MTT [3-(4,5-dimethyl-2-thiazolyl)-2,5-diphenyl-2H-tetrazolium bromide] solution (2 ml) added samples (75 μg/ml) were then nurtured under a humidified atmosphere of 5% CO_2 for 4 h at 37°C. The cell viability was calculated on the spectrophotometric microplate at the optical density (OD) value of 570 nm. Cell morphology was viewed under optical microscopy at 40 μm for 1, 3, 7, and 14 days of experimental periods. For cell viability, three replicated values were averaged.

2.8.3 Cytotoxicity evaluation by luminescence assay

ATP luminescent assay was utilized here to estimate cell proliferation. hBMSCs were treated with various composites for 24 h, and after treatment, the cells were harvested and mixed with equal volumes on ATP buffer reagent and incubated in the dark for 15 min hBMSCs were used as control cells in the absence of any composites. After incubation, the luminescence signals were measured using an ELISA plate reader (Perkin-Elmer, Victor).

2.8.4 Osteogenic differentiation by gene expression studies

Cell phenotype was examined by analyzing mRNA levels using real-time polymerase chain reaction (RT-PCR). The specimens were subjected to PBS washing three times after culturing the specimens for 14 days, and then they were put off in cold TRIzol Reagent (1 ml). The total RNA of each sample was extracted and again put off in RNase-free water (50 μL) using the standard TRIzol protocol (Okamura et al., 2020). Following the protocol, the cDNA was created and stored at -20°C until further analysis. A power SYBR green RT-PCR kit protocol was followed to analyze the PCR quantitatively, and the experiments were conducted in triplicate (n = 3). Osteocalcin (OCN), runt-related transcription factor (RUNx), and vascular endothelial growth factor (VEGF) genes were utilized as osteogenesis markers. The untreated cells were set as control. The sequences of the primers used are listed in Table 1.

2.9 Statistical analysis

The triplicated experiments were averaged and statistically compared with one way ANOVA tool built-in origin pro 8.5. $p < 0.05$ was considered a statistically significant value between the groups.

3 Results and discussion

3.1 Fourier Transform Infra-Red (FT-IR) analysis

The functional groups present in all prepared composites were evaluated using FT-IR analysis, and the results are shown in Figures 1A, B. Figure 1Aa stands for the FT-IR spectrum of pure HAP ceramic. The peaks that appeared here are well-matched with the previous report (Gheisari et al., 2015). The broad peak centered at 3,450 cm^{-1} with the range between 3,700 cm^{-1} to 3,200 cm^{-1} is due to crystalline H-O-H of HAP ceramic. The presence of the small amount of CO_3^{2-} group was confirmed by the appearance of the absorption band at 1,643 cm^{-1}. HAP's phosphate (PO_4^{3-}) groups allocated at 1,029 cm^{-1}, 601 cm^{-1}, and 563 cm^{-1}. In addition, the P-OH stretching mode of vibration was confirmed at the region of 862 cm^{-1}. Thus, Figure 1Aa confirms the formation of HAP ceramic with good functionality. The HAP/COL composite formation was confirmed and produced in Figure 1Ab. The representative peaks of collagen were found along with HAP functional groups. Various absorptions at 1647 cm-1, 1,530 cm-1, 1460 cm-1, and 1,195 cm-1 correspond to amide I- C=O, amide II- N-H stretching, C-N deformation, and amide III-N-H stretching, respectively. Moreover, CH_2 symmetric stretching and–OH bands were observed at 2,929 cm^{-1} and 3,700 cm^{-1} to

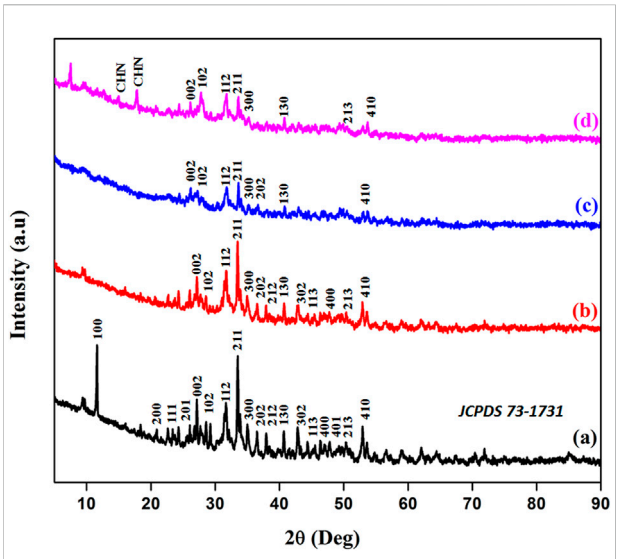

FIGURE 2
XRD patterns of **(A)** HAP ceramic, **(B)** HAP/COL composite, **(C)** HAP/COL/CCQD composite, and **(D)** HAP/COL/CCQD/CRN composite.

3,200 cm^{-1}, respectively. Hydrogen bonding is the probable interaction between collagen's oxygen and nitrogen atoms and hydroxyapatite's hydrogen. Hydrogen bonds occur between the hydrogen atom in collagen and the oxygen atom in hydroxyapatite (Mendes et al., 2012; Siswanto et al., 2020). The HAP's phosphate groups were appeared at 1,116 cm^{-1}, 1,026 cm^{-1}, 601 cm^{-1}, 559 cm^{-1}. The vibration band at 858 cm^{-1} represents the P-OH stretching of HPO_4^{2-}. The slight deviation of peaks from their original region corresponding to COL and HAP functionality may be due to the molecular interaction between COL and HAP compounds, which confirms the formation of HAP/COL composite. The prepared CCQD has functional groups (Figure 1Ba) similar to that reported in previous literature by Kurdekar et al., in 2016 (Kurdekar et al., 2016). In HAP/COL/CCQD composite (Figure 1Ac), the presence of CCQD was confirmed by the characteristic peaks that appeared at 3,450 cm-1, 1,637 cm-1, and 1,080 cm-1 in the carboxylic group, C=O stretching and C–O stretching vibrations of CCQD, respectively. In addition, the peaks at 1560 cm^{-1}, 2,350 cm^{-1}, 1,394 $cm^{-1,}$ and 661 cm^{-1} have also appeared, corresponding to vibration bands of N-H, C≡N (amino groups'), stretching, and bending vibrations C=C and = C-H, respectively (Kurdekar et al., 2016; Sun and Wu, 2018). Here, the absorbance peak at 3,450 cm^{-1} corresponding to carboxylic–OH appeared more sharply than previous composites due to interaction with other components' –OH group. Along with these CCQD functional groups, the HAP and COL functional groups present with slight deviation indicating the formation of HAP/COL/CCQD composite with good interactions. The functional vibrations of pure CRN molecules

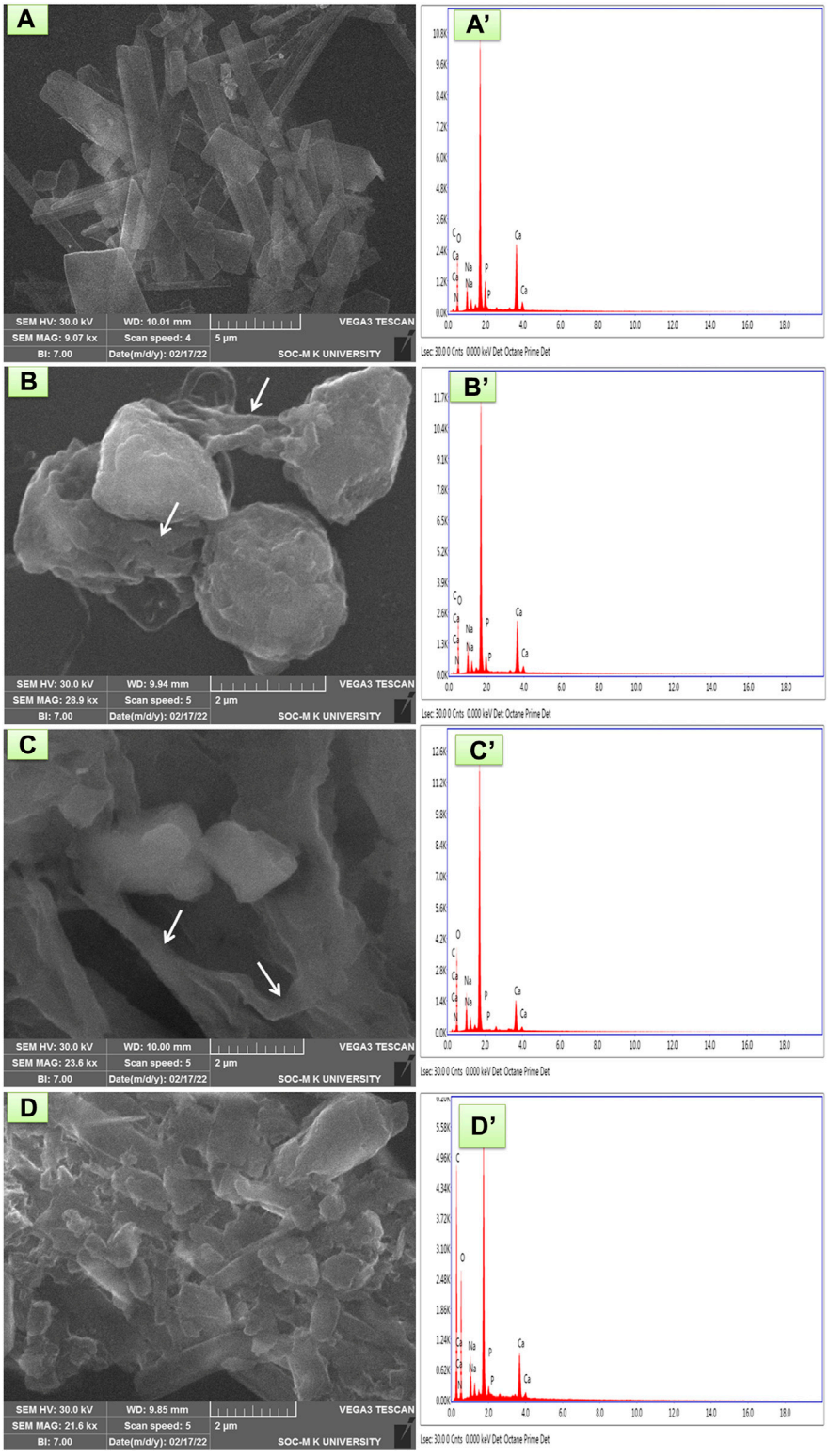

FIGURE 3
SEM and EDX analysis of **(A** and **A')** HAP ceramic **(B** and **B')** HAP/COL composite, **(C** and **C')** HAP/COL/CCQD composite, and **(D** and **D')** HAP/COL/CCQD/CRN composite.

are shown in Figure 1Bb. The terminal–OH functional group of CRN has appeared at 3,408 cm^{-1}. The C–H stretching of -CH group appeared at 2,715 cm^{-1} and 2,627 cm^{-1}. The C=O stretching gave the sharp band at 1653 cm^{-1}. The successive bands within the region of 1500 cm^{-1} to 1370 cm^{-1} are attributed to the C–C–C stretching and C–CO–C bending of the aromatic group. C–O stretch has appeared at 1165 cm^{-1}. The CRN molecule FT-IR results agree with those of Sulaiman et al. report (Sulaiman et al., 2018). In the composite, less difference has occurred between the pure CRN and CRN in HAP/COL/CCQD composite. As shown in Figure 1Ad, the characteristic peaks of HAP, COL, CCQD, and CRN components appeared slightly from their original position, representing the successful physical interaction of CRN and HAP, thus finally confirming the CRN-loaded HAP/COL/CCQD composite formation.

3.2 Phase analysis

After the composite formation, the X-ray diffraction analyses of HAP ceramic, HAP/COL composite, HAP/COL/CCQD composite, and HAP/COL/CCQD/CRN composite were carried out. The results are given in Figure 2. In addition to the FT-IR spectrum, HAP ceramic formation was confirmed by analyzing its phase nature by the XRD instrument. The XRD patterns of HAP (JCPDS 73–1731) have been shown in Figure 2A. According to this pattern, the entire characteristic peaks of HAP at the two theta values and their corresponding planes of 11.6° (100), 22.6° (200), 24.2° (111), 26° (201), 27° (002), 29.2° (102), 31.6° (112), 33.5° (211), 35° (300), 36.4° (202), 38° (212), 40.6° (130), 42.8° (302), 44.3° (113), 46.4° (400), 47.6° (401), 50.42° (213) and 53° (410) were observed which denotes the formation of pure HAP with well crystalline nature (You et al., 2019). The higher intensity of the 100 plan is due to the cutting planes being close to the hydroxyl column ((100) a/b type) or between the phosphate-rich layers ((100) c/c type) or Ca1 ion redistributed type ((100) d/e type) (Pan et al., 2007). After the COL addition with HAP ceramic and the formation of HAP/COL composite, it did not affect the crystallinity of the HAP ceramic. The observed patterns are well crystalline, with the disappearance of some peaks due to COL interaction (Figure 2B). After the CCQD addition, it slightly affects the crystallinity of the HAP ceramic, evidenced by the broadened peaks of HAP ceramic in Figure 2C. It may be due to the amorphous nature of the carbon dots (Puvvada et al., 2012). Two new sharp peaks at the two theta of 12.7° and 17.7° appeared in Figure 2D for the HAP/COL/CCQD/CHN composite due to the presence of CHN molecule on the composite (Prabakaran and Rajan, 2021).

Moreover, the average crystallite sizes of HAP ceramic were calculated in its pure form and its composite form using the Debye Scherrer equation. The observed crystallite sizes of HAP in HAP ceramic, HAP/COL, HAP/COL/CCQD, and HAP/COL/CCQD/CHN composites were calculated as ~ 8.6 nm, ~ 7.4 nm, ~ 6.9 nm, and ~6.6 nm, respectively. Adding extra organic compounds into HAP ceramic has influenced the crystal growth of HAP and decreased its crystallite size. It may be due to various functional groups in COL and CCQD compounds interacting with HAP ceramic and affecting its crystal growth. But the addition of the CHN molecule on the HAP/COL/CCQD composite did not alter the crystal growth of HAP. It remained crystallite like in HAP/COL/CCQD composite and did not vary hugely.

3.3 Morphology by SEM analysis

The morphology of prepared composites was evaluated and presented in Figure 3. The rod-like HAP was formed, as evidenced by Figure 3A. The rod-like morphology occurred due to the growth of HAP crystals along the straight and forward direction with a rod length of ~7.4 μm. The experiment's temperature and chosen pH did not affect this HAP crystal growth. Moreover, the growth of HAP crystals was favored by the absence of external moieties.

In contrast, adding any organic materials such as COL, CCQD, and CRN has completely changed the rod morphology of HAP. In HAP/COL composite, as shown in Figure 3B, the spherical and interconnected fibrils network (denoted by arrows) was obtained. It may be due to the presence of COL fibrils, their interaction with HAP ceramic, and their influence on the growth of HAP crystals. Kaji et al. confirmed this interconnecting fibril structure of COL in 2017 (Kajii et al., 2017). The addition of CCQD in the HAP/COL composite also affected the spherical nature of the HAP/COL composite. But the interconnected fibrils were also presented without any changes (Figure 3C). But the addition of CRN molecule on the HAP/COL/CCQD composite produced the compact arrangement morphology containing some fingers-like rods of CRN molecules in Figure 3D (Prabakaran and Rajan, 2021). Moreover, the composite formation was confirmed by an analysis of elements present in the particular composite by EDX measurements, and the results were presented in Figures 3A'–D'. In HAP ceramic, the atomic weight percentage of Ca and P is 40.70 and 6.00, respectively. Likely, the atomic weight percentage of Ca and P in HAP/COL composite, HAP/COL/CCQD composite, and HAP/COL/CCQD/CRN composite is calculated as 36.61 and 3.40, 23.46 and 0.11, and 10.62 and 0.35, respectively. These data indicate the presence of Ca and P minerals in all the composites appropriately. Moreover, the atomic ratio of Ca and P was also decreased when adding external organic material to form the composite, decreasing the atomic weight percentage of Ca and P ions in the composite (Predoi et al., 2019).

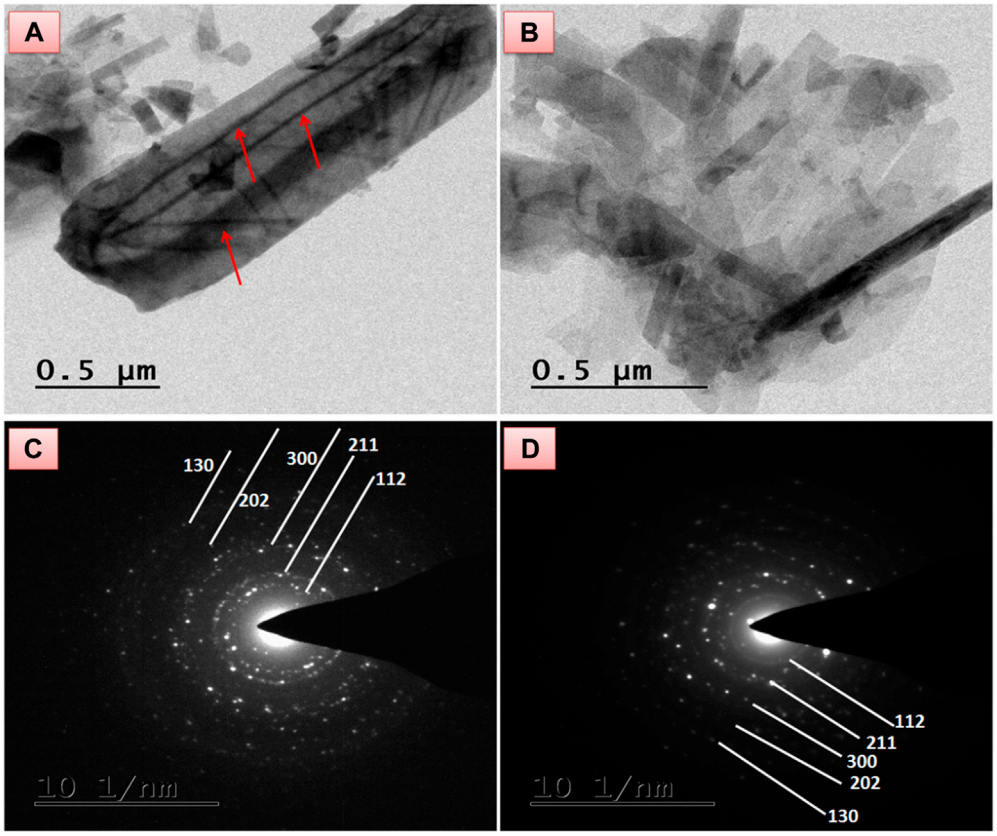

FIGURE 4
TEM morphology of **(A)** HAP/COL/CCQD composite **(B)** HAP/COL/CCQD/CRN composite, and the SAED pattern of **(C)** HAP/COL/CCQD composite, **(D)** HAP/COL/CCQD/CRN composite.

3.4 TEM analysis

Along with SEM observation, the TEM micrograph of HAP/COL/CCQD and HAP/COL/CCQD/CRN composites also reveal the corresponding surface morphologies. Figure 4A stands for surface ultrastructure morphology of HAP/COL/CCQD composite. A fibril structure of triple spirals with ~1.8 μm length (Straight line along with HAP rods) was observed for the collagen molecule in HAP rods. In TEM, crosswise with an average length of ~439 nm and a straight line structure inside the HAP rod is the characteristic collagen fiber, produced by interconnected paralleling of collagen fibrils (indicated by red arrows). The presence of CCQD has appeared as smaller dots beside the HAP rods.

On the other hand, the CRN added composite in Figure 4B shows slightly distorted morphology compared with HAP/COL/CCQD composite. The collagen fibrils are completely distorted, and the HAP rods are retained within the composite. The CRN addition was shaped by the compact arrangement of the composite containing some fingers-like rods of the combination of the HAP rods and CRN molecule in Figure 4B. The average length of HAP rods in HAP/COL/CCQD composite was calculated as ~932 nm. In contrast, the average length of HAP rods in HAP/COL/CCQD/CRN composite was found as ~459 nm. This decreased length of the HAP rods and the complete disappearance of collagen fibrils in the HAP/COL/CCQD/CRN composite may be due to the interaction of the CRN molecule with the HAP composite. Thus, the addition of CRN molecules could affect the morphology structure and growth of the HAP rods, as shown in the XRD results, which were confirmed. Their SAED pattern is given in Figures 4C, D both show the crystalline nature of the composites. The CRN addition does not affect the crystalline nature of the composite due to its crystalline nature, as discussed in the XRD section.

3.5 Particle size analysis

The influence of various components on the physical growth of the various composites, including HAP ceramic, HAP/COL, HAP/COL/CCQD, and HAP/COL/CCQD/CRN, was analyzed

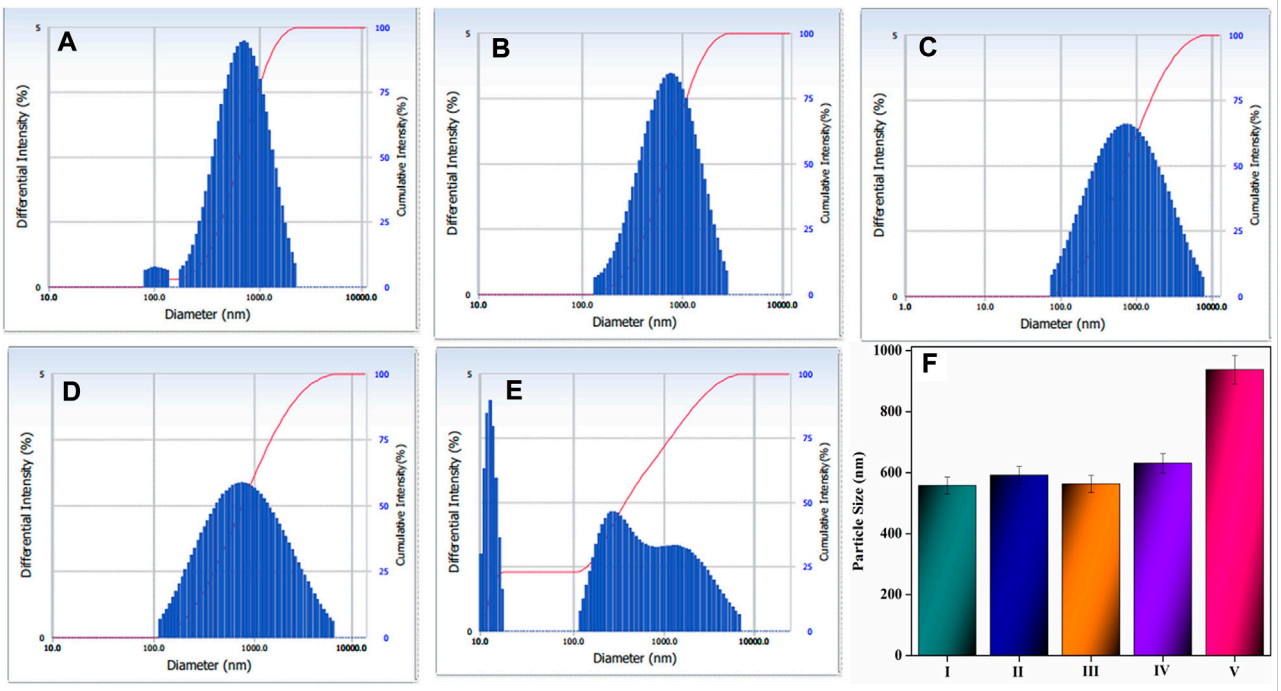

FIGURE 5
Particle size distribution curve of **(A)** pure HAP ceramic, **(B)** pure CCQD, **(C)** HAP/COL composite, **(D)** HAP/COL/CCQD composite, **(E)** HAP/COL/CCQD/CRN composite and **(F)** bar diagram represents the cumulant particle size of all composites including (I) pure HAP ceramic (II) pure CCQD, (III) HAP/COL composite (IV) HAP/COL/CCQD composite, and (IV) HAP/COL/CCQD/CRN composite.

in a particle size measurement. It was recognized by an increase in particle size for the composites prepared with various components due to various chemical interactions between the members in the composite. The cumulant particle sizes were observed as 558.2 nm, 591.8 nm, 563.1 nm, 631.0 nm, and 938.0 nm corresponding to pure HAP, pure CCQD, HAP/COL composite, HAP/COL/CCQD composite, and HAP/COL/CCQD/CRN composite, respectively. The ionic interactions between the HAP and CCQD have increased the particle size of the composite. Similarly, the hydrogen bonding interaction between the HAP/COL/CCQD and CRN molecule has also increased the particle size of the composite. The detailed chemical reaction is discussed in Scheme 1. The lesser particle size within this range (>1 μm) may give a superior homogeneity of the distribution of particles, and superior bonding between the individual components of the composite, and it could increase the density of the composite (Oh et al., 1998; Pramono et al., 2022). Therefore, it is a critical factor that defines the composite's quality. Because of these different particle sizes, the composite aggregates, rather than individual crystallites, might be acting differently in chemical and biochemical reactions (Barabás et al., 2013). Figure 5 describes the particle size distribution curves of the composites. It should be noted that the particle size of the final HAP/COL/CCQD/CRN composite is significantly greater than pure HAP ceramic. The less aggregated smaller particles in "crystal fusion" *via* the drying process in a strong crystal-crystal interaction process easily interact with other components. This crystal fusion process may increase the final composite's particle size containing various individual components (Iafisco et al., 2010).

3.6 Drug entrapment efficiency, loading capacity, and *in-vitro* release profile

The drug entrapment efficiency and loading capacity CRN from HAP/COL/CCQD composite carrier. CRN's entrapment and loading capacity is 65.17%, and 56.24% was attained, as shown in Figure 6A. The entrapment efficiency of CRN was maximum achieved on HAP/COL/CCQD for 24 h *via* physical interaction and π-π stacking interaction of CRN, CCQDs, and HAP. The resultant absorbance peaks of CRN drug were decreased after 1 h. Only very low-intensity absorbance peaks have appeared, showing that CRN drugs were loaded efficiently on the HAP/COL/CCQD composite.

The *in-vitro* discharge outline of any drug delivery system is one of the most vital physicochemical features for forecasting their *in-vivo* performance, connecting it to the structure of the formed carrier, and planning preparations of the composite with the anticipated possessions. In the current work, continuous

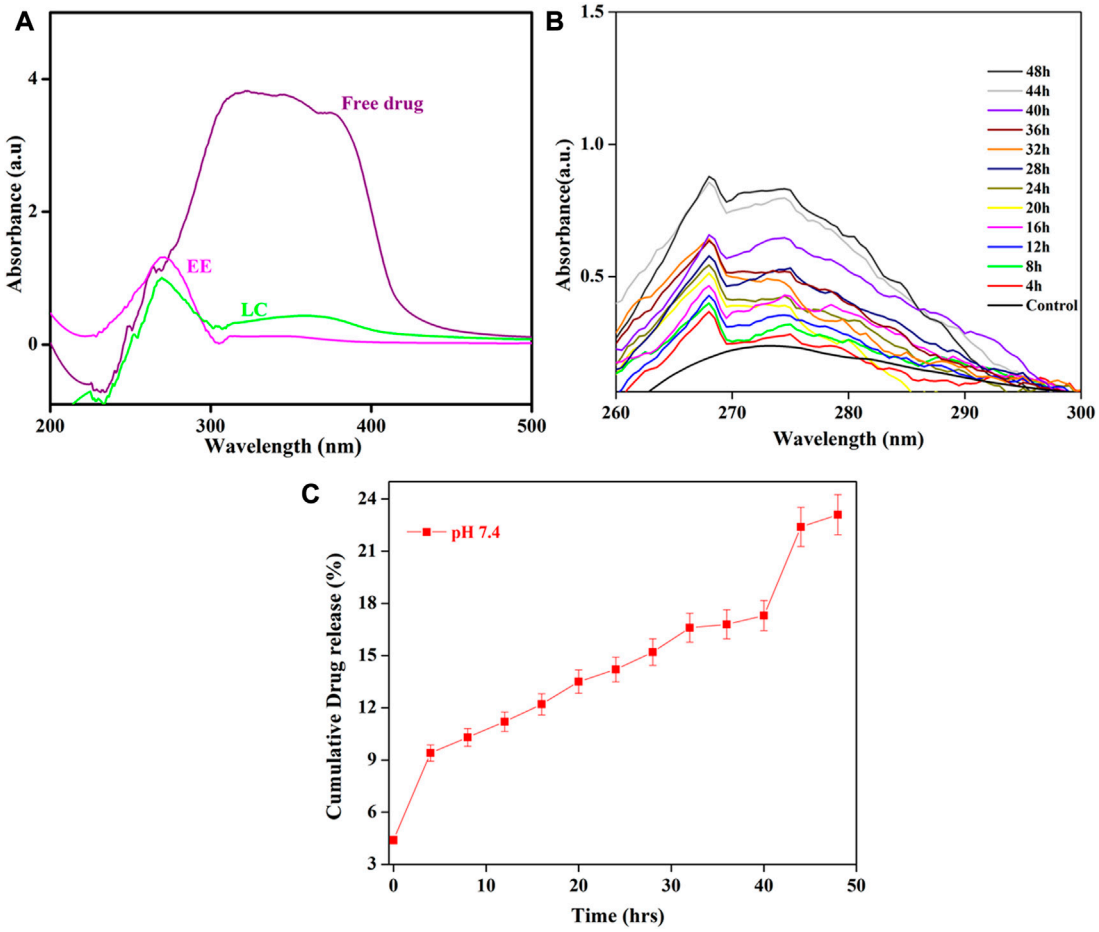

FIGURE 6
(A) Drug loading capacity and entrapment efficiency of HAP/COL/CCQD/CRN composite **(B)** *In vitro* drug release profile of HAP/COL/CCQD/CRN composite and **(C)** cumulative releasing profile of CRN drug from HAP/COL/CCQD/CRN composite.

release of the CRN from the HAP/COL/CCQD/CRN composite was the highest percentage in the HAP/COL/CCQD/CRN formulation, which suggested enhanced entrapment of CRN with that composite formulation. Figure 6 shows the discharge performance of the CRN drug in PBS medium at the pH of 7.4 from the HAP/COL/CCQD/CRN composite. The maximum CRN, i.e., ~23%, was released from the composite for 50 h (Figure 6C). In this case, no burst release was observed for the first few hours. Only the controlled slow-release was obtained. This strongly shows CRN molecule's loading on HAP/COL/CCQD carrier. Thus, the present research achieved the prolonged release of CRN and slower release kinetics when HAP/COL/CCQD/CRN composite formulation was used. This may be connected to constructing a tougher complex due to the surplus electrostatic interaction of the HAP/COL/CCQD composite with hydroxyl groups on the CRN molecule.

This releasing percentage was significantly lower than the releasing percentage of CRN drug from the β-cyclodextrin (β-CD)-based nanosponge (NS) polymers formulation developed by Mahalingam et al., in 2017. They evaluated that the CRN releasing behavior from the β-CD-NS formulation was about 59% for 36 h. In our case, we have obtained only the ~23% of CRN release from the composite for 48 h. This result indicates that the interaction between the CRN and HAP/COL/CCQD composite is stronger than the interaction between the CRN and NS polymer that was prepared by Mahalingam et al. (Mahalingam et al., 2017). Shima et al., in 2020, CHR (chrysin) discharge from electrospun PCL/GEL fibers with various CHR contents was reported. In pH 7.4 at 37°C, CHR was released from electrospun fibers at 5% and 15% (wt:wt%) for 24 h and continued by low drug discharge was determined *via* 2 weeks. After 2 weeks, almost 92% and 78% of CHR were discharged from 5% to 15% (wt:wt%) CHR-loaded fibers (Sadeghi-Soureh et al., 2020). Further, cumulative drug release profiles represent Figure 6C the maximum amount of drug release was observed at pH-7.4 in 23.11%, in alkaline

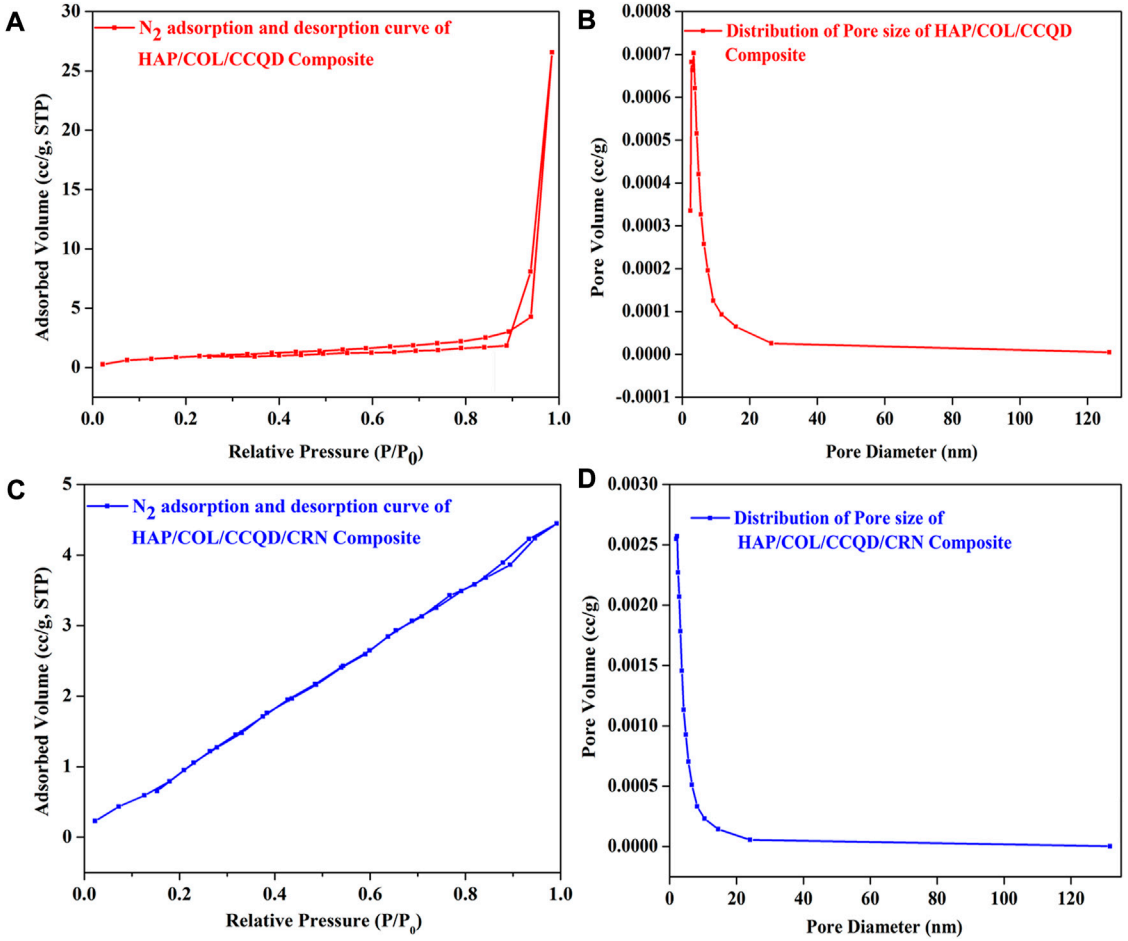

FIGURE 7
(A) N_2 adsorption and desorption isotherm of HAP/COL/CCQD composite, **(B)** N_2 adsorption and desorption isotherm of CRN loaded HAP/COL/CCQD composite, **(C)** Pore size distribution curve of HAP/COL/CCQD composite and **(D)** Pore size distribution curve of CRN loaded HAP/COL/CCQD composite.

pH conditions, the free hydrophilic groups of HAP/COL/CCQD/CRN composite help to the formation of hydrogen bond with a water molecule and allow the fast discharge inside the affected tissues and sustainably release of CRN drugs molecule.

3.7 Specific surface area and pore size distribution

In order to get the effect of CRN molecule on the surface area and pore size distribution of both HAP/COL/CCQD and HAP/COL/CCQD/CRN composites, the BET analysis was carried out using N_2 gas adsorption, and the results were compared. It has been identified that the surface area increases as the loading of CRN molecule in HAP/COL/CCQD composite. It was calculated that the surface area, pore diameter, and pore volume of HAP/COL/CCQD composite are 2.720 m^2/g, 0.004 cc/g, and 3.400 nm, respectively. The CRN-loaded composite exhibits 9.209 m^2/g, 0.009 cc/g, and 2.247 nm for the surface area, pore diameter, and pore volume. Figures 7A, B shows that type-III isotherm with hysteresis loop was observed for both HAP/COL/CCQD and HAP/COL/CCQD/CRN composites. It is supposed that the addition of external molecules on the surface of the composite generates atomic-scale heterogeneity and unevenness, which might have produced increases in the surface area and decreases in pore volume, as discussed by Ain et al. (Ul Ain et al., 2020). At the same time, both composites exhibit mesoporous nature because the maximum pores are cumulated within the range of 2–20 nm (Figures 7C, D). A large surface area with a high pore volume, a tunable mesoporous structure, high mechanical and chemical stability, and biocompatibility for biomedical applications (Purbia and Paria, 2015; Shaikh et al., 2016).

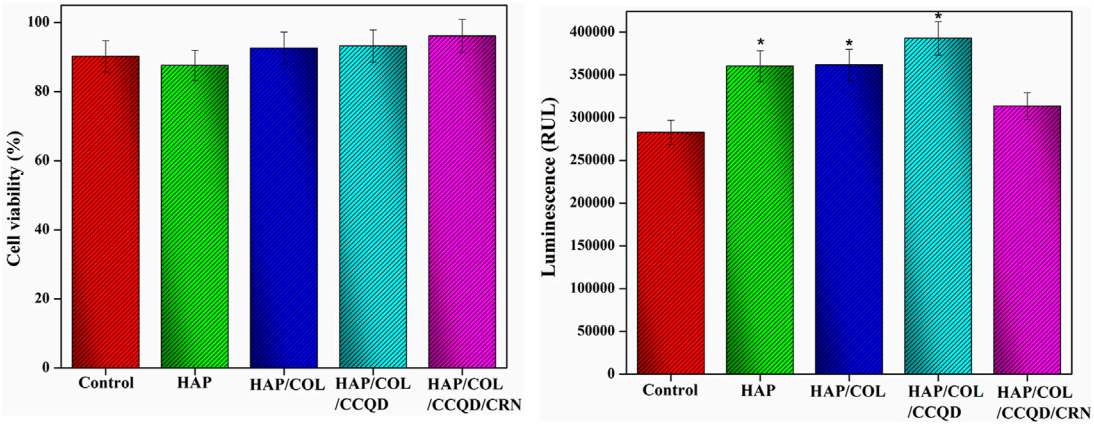

FIGURE 8
(A,B) Viability and cytotoxicity nature of the hBMSCs after treated with (a) pure HAP ceramic (b) HAP/COL composite, (c) HAP/COL/CCQD composite, and (d) HAP/COL/CCQD/CRN composite 14 days of post culturing period. *$p < 0.05$ comparison of the experimented group with the control cells.

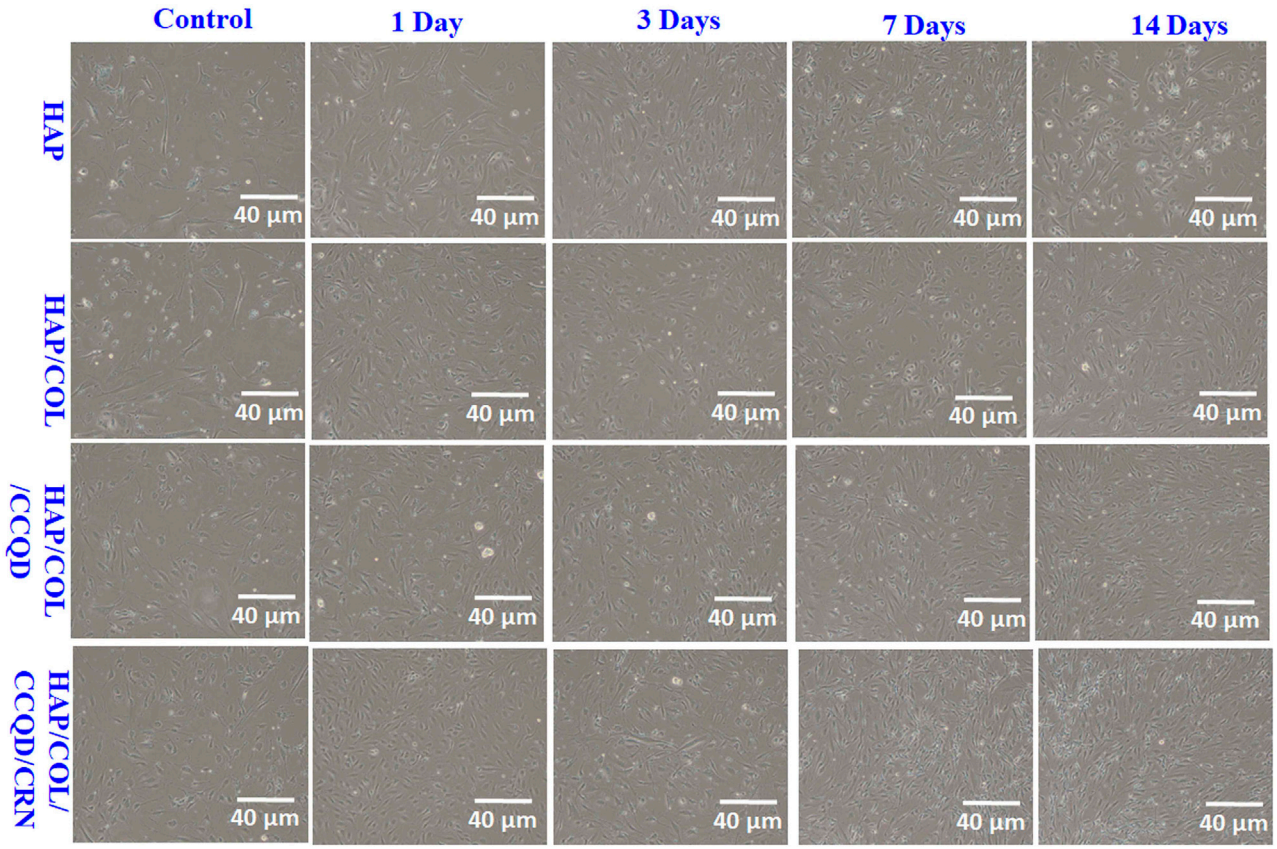

FIGURE 9
Optical microscopic images of hBMSCs after being treated with prepared composites at different treatment days.

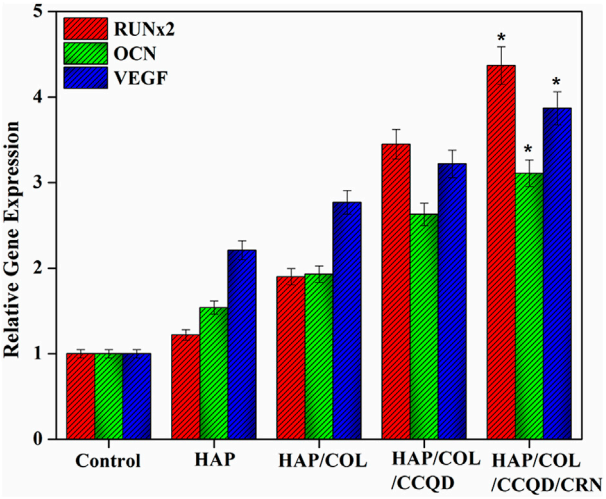

FIGURE 10
Relative gene expression behavior of hBMSCs after treatment with **(A)** pure HAP ceramic **(B)** HAP/COL composite, **(C)** HAP/COL/CCQD composite, and **(D)** HAP/COL/CCQD/CRN composite 14 days of post culturing period. *$p < 0.05$ comparison of the experimented group with the control groups.

3.8 Biological characterizations

3.8.1 Cell viability, cytotoxicity and morphology

The attachment and proliferation of hBMSCs were examined to estimate whether the prepared composites fulfilled the necessity in bone tissue engineering and how the additional organic compounds in the composite play a role in cellular metabolism. An effect of HAP, HAP/COL, HAP/COL/CCQD, and HAP/COL/CCQD/CRN on the metabolic activity of the hBMSCs was evaluated in terms of MTT and luminescence assays 14 days of post culturing period and given in Figure 8. All composites exhibit good support to the hBMSCs growth. There was no significant difference observed in the MTT assay between the control (blank untreated cells) and HAP, HAP/COL, and HAP/COL/CCQD composites treated cells (Figure 8A). But after the treatment of cells with HAP/COL/CCQD/CRN composite, it has enhanced the viability of the cells and reached a maximum up to 96%, which is slightly higher than the other composites such as HAP (87.6%), HAP/COL (92.6%) and HAP/COL/CCQD (93.2%). None of the composites shows similar viability results to control cells. Adding organic compounds such as COL, CCQD, and CRN molecules did not affect the growth of hBMSCs and induced a positive effect on the proliferation of hBMSCs. Moreover, the cytotoxicity of the HAP/COL/CCQD/CRN composite on the hBMSCs is nearly equal to control cells (Figure 8B). On the other hand, the other composites, such as HAP, HAP/COL, and HAP/COL/CCQD, have induced some cytotoxicity effects than HAP/COL/CCQD/CRN and control cells. These results prove the cytocompatibility nature of the prepared composites.

In addition, the cytocompatibility nature of the composite was also well evidenced by the optical microscopic morphology of hBMSCs obtained at 1, 3, 7, and 14 days of post-treatment with prepared composites (Figure 9). Other than the control cells, the cells were attached compactly and covered the surface of culture dishes in all other experimented groups. In particular, the composites at 14 days post-culture period exhibit more cells in a tightly bounded manner than other treatment days observed. The final composite containing CRN molecule shows more prolonged spindle-shaped cells than other composites at 7 and 14 days of culture. This may be due to the initial attachment of cells that could interact with the surface of the composite, and the presence of various compounds in the composites can allow cells to attach to the composite. This is the basis for the cell viability of the experimental composite, as discussed by Genasan Krishnamurithy in 2019 (Krishnamurithy et al., 2019).

3.8.2 Osteogenic differentiation by relative gene expressions

To assess the differentiation manners of hBMSCs on the composite with diverse compounds, relative genes expression like RUNx2, OCN, and VEGF measurements are indispensable. OCN is a characteristic indicator of the bio-mineralization behavior of bone and developed osteoblasts. As shown in Figure 10, adding organic molecules such as COL, CCQD, and CRN does not negatively affect the gene expression levels. Moreover, hBMSCs exhibit higher OCN expression levels than the control group on all composites. In addition, on the 14th day, the cells on the composite's surface containing CRN molecules showed significantly higher OCN expression levels. In addition, like OCN expression results, the other genes, such as RUNx2 and VEGF expressions, showed significantly higher upregulated when the expression on the CRN-containing composite. Other composites such as HAP, HAP/COL, and HAP/COL/CCQD show relatively downregulated expression of all genes, including OCN, RUNx2, and VEGF, compared with HAP/COL/CCQD/CRN composite. These upregulated gene expressions for CRN-containing composite may be due to the CRN molecule's ERK/MAPK activation. The fundamental molecular mechanism shows that ERK1/2 is responsible for the inductive effects of chrysin (Zeng et al., 2013), making the CRN molecule an osteogenic molecule for treating bone diseases, including osteoporosis. Prominent expression of OCN, RUNx2, and VEGF in cells seeded in the HAP/COL/CCQD/CRN composite specifies that this scaffold is appropriate for the osteogenic induction and quick osteogenic differentiation of seeded hBMS cells (Genasan et al., 2021).

4 Conclusion

In this examination, composites with bioactive compounds were prepared using the chemical precipitation technique controlled by the solvent removal method. The surface of HAP scaffolds was utilized to examine the combining effects of bioactive compounds on the morphology, crystal growth, adhesion, and viable behavior of hBMSCs. The results displayed that HAP scaffolds with COL/CCQD/CRN compounds were more positive for the spread of cells than other individual composites. In addition, the CRN molecule on the composite hastened the surface area of the HAP/COL/CCQD composite and gifted the composite with a better ability to express and upregulated bone cells, as proved by the MTT assay and osteoblasts cells' gene expression. The composite made up of HAP/COL/CCQD/CRN compounds exhibited significantly higher cell proliferation rate and gene expression rate among other composites, showing the cytocompatibility nature of the CRN molecule combined with HAP ceramic. This CRN-containing composite is more promising for skeletal tissue engineering than other composites that do not contain CRN molecules. More detailed preclinical examinations on the composite's degradation and *in vivo* bone tissue development continue to recognize the translational probable of this composite.

Data availability statement

The datasets presented in this study can be found in online repositories. The names of the repository/repositories and accession number(s) can be found in the article/supplementary material.

Author contributions

Conception and design of study: BC and YH Acquisition of data: AZ, SC, SM, YA, and MJ Analysis and/or interpretation of data: AZ, SC, SM, YA, MJ, BC and YH.

Funding

Natural Science Foundation of Chongqing municipality, cstc2020jcyj-msxmX0084 and the authors would like to thank the Deanship of Scientific Research, Majmaah University, Kingdom of Saudi Arabia for research support under the project number: *R-2022-303*.

Conflict of interest

The authors declare that the research was conducted in the absence of any commercial or financial relationships that could be construed as a potential conflict of interest.

Publisher's note

All claims expressed in this article are solely those of the authors and do not necessarily represent those of their affiliated organizations, or those of the publisher, the editors and the reviewers. Any product that may be evaluated in this article, or claim that may be made by its manufacturer, is not guaranteed or endorsed by the publisher.

References

Antoniac, I. V., Antoniac, A., Vasile, E., Tecu, C., Fosca, M., Yankova, V. G., et al. (2021). *In vitro* characterization of novel nanostructured collagen-hydroxyapatite composite scaffolds doped with magnesium with improved biodegradation rate for hard tissue regeneration. *Bioact. Mater.* 6, 3383–3395. doi:10.1016/j.bioactmat.2021.02.030

Barabás, R., Czikó, M., Dékány, I., Bizo, L., and Sára Bogya, E. (2013). Comparative study of particle size analysis of hydroxyapatite-based nanomaterials. *Chem. Pap.* (67), 1414–1423. doi:10.2478/s11696-013-0409-6

Bharati, S., Sinha, M. K., and Basu, D. (2005). Hydroxyapatite coating by biomimetic method on titanium alloy using concentrated SBF. *Bull. Mat. Sci.* 28, 617–621. doi:10.1007/bf02706352

David, M. (2020). in *Nunamaker, orthopedic implant failure, equine fracture repair*. Editor A. J. Nixon. Second Edition (John Wiley & Sons).

Fratzl, P., and Weinkamer, R. (2007). Nature's hierarchical materials. *Prog. Mat. Sci.* 52, 1263–1334. doi:10.1016/j.pmatsci.2007.06.001

Fu, Z., Cui, J., Zhao, B., Shen, S. G. F., and Lin, K. (2021). An overview of polyester/hydroxyapatite composites for bone tissue repairing. *J. Ortho. Transl.* 28, 11–130.

Genasan, K., Mehrali, M., Veerappan, T., Talebian, S., Malliga Raman, M., Singh, S., et al. (2021). Calcium-silicate-incorporated gellan-chitosan induced osteogenic differentiation in mesenchymal stromal cells. *Polymers* 13, 3211. doi:10.3390/polym13193211

Gheisari, H., Karamian, E., and Abdellahi, M. (2015). A novel hydroxyapatite–Hardystonite nanocomposite ceramic. *Ceram. Int.* 41, 5967–5975. doi:10.1016/j.ceramint.2015.01.033

Ghorghi, M., Rafienia, M., Nasirian, V., Bitaraf, F. S., Gharravi, A. M., and Zarrabi, A. (2020). Electrospun captopril-loaded PCL-carbon quantum dots nanocomposite scaffold: Fabrication, characterization, and *in vitro* studies. *Polym. Adv. Technol.* 31 (12), 1–14. doi:10.1002/pat.5054

Haritha Menon, A., Preethi Soundarya, S., Sanjay, V., Viji Chandran, S., Balagangadharan, K., and Selvamurugan, N. (2018). Sustained release of chrysin from chitosan-based scaffolds promotes mesenchymal stem cell proliferation and osteoblast differentiation. *Carbohydr. Polym.* 195, 356–367. doi:10.1016/j.carbpol.2018.04.115

Heydari, Z., Mohebbi-Kalhori, D., and Shafiee Afarani, M. (2017). Engineered electrospun polycaprolactone (PCL)/octacalcium phosphate (OCP) scaffold for bone tissue engineering. *Mater. Sci. Eng. C* 81, 127–132. doi:10.1016/j.msec.2017.07.041

Iafisco, M., Varoni, E., Battistella, E., Pietronave, S., Prat, M., Roveri, N., et al. (2010). The cooperative effect of size and crystallinity degree on the resorption of biomimetic hydroxyapatite for soft tissue augmentation. *Int. J. Artif. Organs* 33 (11), 765–774. doi:10.1177/039139881003301101

Ingole, V. H., Ghule, S. S., Vuherer, T., Kokol, V., and Ghule, A. V. (2021). Mechanical properties of differently nanostructured and high-pressure compressed hydroxyapatite-based materials for bone tissue regeneration. *Minerals* 11, 1390. doi:10.3390/min11121390

Jeong, J., Hun Kim, J., Hee Shim, J., Hwang, N. S., and Yeong Heo, C. (2019). Bioactive calcium phosphate materials and applications in bone regeneration. *Biomater. Res.* 23 (4), 4–11. doi:10.1186/s40824-018-0149-3

Kajii, F., Iwai, A., Tanaka, H., Matsui, K., Kawai, T., and Kamakura, S. (2017). Influence of electron beam irradiation doses on bone regeneration by octacalcium phosphate collagen composites. *J. Tissue Eng. Regen. Med.* 12, e1186–e1194. doi:10.1002/term.2505

Kamakura, S., Sasaki, K., Honda, Y., Anada, T., and Suzuki, O. (2006). Octacalcium phosphate combined with collagen orthotopically enhances bone regeneration. *J. Biomed. Mat. Res.* 79 (2), 210–217. doi:10.1002/jbm.b.30531

Kawai, T., Anada, T., Honda, Y., Kamakura, S., Matsui, K., Matsui, A., et al. (2009). Synthetic octacalcium phosphate augments bone regeneration correlated with its content in collagen scaffold. *Tissue Eng. Part A* 15, 23–32. doi:10.1089/ten.tea.2008.0141

Kim, T., Wang See, C., Li, X., and Zhu, D. (2020). Orthopedic implants and devices for bone fractures and defects: Past, present and perspective. *Eng. Regen.* 1, 6–18. doi:10.1016/j.engreg.2020.05.003

Kręcisz, B., Kieć-Świerczyńska, M., and Bąkowicz-Mitura, K. (2006). Allergy to metals as a cause of orthopedic implant failure. *Int. J. Occup. Med. Environ. Health* 19 (3), 178–180. doi:10.2478/v10001-006-0025-6

Krishnamurithy, G., Mohan, S., Yahya, N. A., Mansor, A., Murali, M. R., Raghavendran, H. R. B., et al. (2019). The physicochemical and biomechanical profile of forsterite and its osteogenic potential of mesenchymal stromal cells. *PLOS ONE* 14, e0214212. doi:10.1371/journal.pone.0214212

Kurdekar, A., Chunduri, L. A. A., Bulagonda, E. P., Haleyurgirisetty, M. K., Kamisetti, V., and Hewlett, I. K. (2016). Comparative performance evaluation of carbon dot based paper immunoassay on Whatman filter paper and Nitrocellulose paper in the detection of HIV infection. *Microfluid. Nanofluidics* 20, 99. doi:10.1007/s10404-016-1763-9

Levingstone, T. J., Herbaj, S., and Dunne, N. J. (2019). Calcium phosphate nanoparticles for therapeutic applications in bone regeneration. *Nanomaterials* 9 (11), 1570–1622. doi:10.3390/nano9111570

Lim, S. Y., Shen, W., and Gao, Z. (2015). Carbon quantum dots and their applications. *Chem. Soc. Rev.* 44, 362–381. doi:10.1039/c4cs00269e

Luo, P. G., Sahu, S., Yang, S. T., Sonkar, S. K., Wang, J., Wang, H., et al. (2013). Carbon "quantum" dots for optical bioimaging. *J. Mat. Chem. B* 1, 2116–2127. doi:10.1039/c3tb00018d

Ma, G. (2019). Three common preparation methods of hydroxyapatite. *IOP Conf. Ser. Mat. Sci. Eng.* 688, 033057. doi:10.1088/1757-899x/688/3/033057

Mahalingam, S., Thomas, Philip A., Karuppasamy, V., Jeganathan, K., and Pitchairaj, G. (2017). NF1 and neurofibromin: Emerging players in the genetic landscape of desmoplastic melanoma. *Adv. Anat. Pathol.* 24 (17), 1–14. doi:10.1097/PAP.0000000000000131

Mendes, L. C., Ribeiro, G. L., and Marques, R. C. (2012). <i>*in situ*</i> hydroxyapatite synthesis: Influence of collagen on its structural and morphological characteristic. *Mater. Sci. Appl.* 03 (3), 580–586. doi:10.4236/msa.2012.38083

Min Kim, J., Suk Yang, Y., Hwan Park, K., Oh, H., Greenblatt, M. B., and Hyuck Shim, J. (2019). The ERK MAPK pathway is essential for skeletal development and homeostasis. *Int. J. Mol. Sci.* 20 (8), 1803. doi:10.3390/ijms20081803

Oh, S. T., Sekino, T., and Niihara, K. (1998). Effect of particle size distribution and mixing homogeneity on microstructure and strength of alumina/copper composites. *Nanostructured Mater.* 10, 327–332. doi:10.1016/s0965-9773(98)00072-5

Okamura, K., Inagaki, Y., Matsui, T. K., Matsubayashi, M., Komeda, T., Ogawa, M., et al. (2020). RT-qPCR analyses on the osteogenic differentiation from human iPS cells: An investigation of reference genes. *Sci. Rep.* 10, 11748. doi:10.1038/s41598-020-68752-2

Pan, H., Tao, J., Xu, X., and Tang, R. (2007). Adsorption processes of gly and glu amino acids on hydroxyapatite surfaces at the atomic level. *Langmuir* 23 (17), 8972–8981. doi:10.1021/la700567r

Prabakaran, S., Rajan, M., Geng, Z., and Liu, Y. (2021). Fabrication of substituted hydroxyapatite-starch-clay bio-composite coated titanium implant for new bone formation. *Carbohydr. Polym.* 271, 118432. doi:10.1016/j.carbpol.2021.118432

Prabakaran, S., and Rajan, M. (2021). The osteogenic and bacterial inhibition potential of natural and synthetic compound loaded metal–ceramic composite coated titanium implant for orthopedic applications. *New J. Chem.* 45, 15996–16010. doi:10.1039/d1nj02363b

Pramono, A., Ensang Timuda, G., Pramudya Ahmad Rifai, G., and Shidqi Khaerudini, D. (2022). Synthesis of spinel-hydroxyapatite composite utilizing bovine bone and beverage can. *Crystals* 12, 96. doi:10.3390/cryst12010096

Predoi, D., Liliana Iconaru, S., Valentin Predoi, M., Motelica-Heino, M., Guegan, R., and Buton, N. (2019). Evaluation of antibacterial activity of zinc-doped hydroxyapatite colloids and dispersion stability using ultrasounds. *Nanomaterials* 9, 515. doi:10.3390/nano9040515

Purbia, R., and Paria, S. (2015). Yolk/shell nanoparticles: Classifications, synthesis, properties, and applications. *Nanoscale* 7, 19789–19873. doi:10.1039/c5nr04729c

Puvvada, N., Prashanth Kumar, B. N., Konar, S., Kalita, H., Mandal, M., and Pathak, A. (2012). Synthesis of biocompatible multicolor luminescent carbon dots for bioimaging applications. *Sci. Technol. Adv. Mat.* 13, 045008–45017. doi:10.1088/1468-6996/13/4/045008

Rafienia, M., Nasirian, V., Mansouri, K., and Vaisi-Raygani, A. (2018). Methotrexate conjugated to polymer quantum dot for cytotoxicity effect improved against MCF-7 and Hela cells. *Med. Chem. Res.* 27, 1578–1588. doi:10.1007/s00044-018-2173-1

Reddy Kasala, E., Narendra Bodduluru, L., Mohanrao Madana, R., Athira, K. V., Gogoi, R., and Barua, C. C. (2015). Chemopreventive and therapeutic potential of chrysin in cancer: Mechanistic perspectives. *Toxicol. Lett.* 233, 214–225. doi:10.1016/j.toxlet.2015.01.008

Sadeghi-Soureh, S., Jafari, R., Gholikhani-Darbroud, R., and Pilehvar Soltanahmadi, Y. (2020). Potential of Chrysin-loaded PCL/gelatin nanofibers for modulation of macrophage functional polarity towards anti-inflammatory/pro-regenerative phenotype. *J. drug Deliv. Sci. Technol.* 58, 101802. doi:10.1016/j.jddst.2020.101802

Shaikh, S. F., Mane, R. S., Koun Min, B., Jeong Hwang, Y., and Shim Joo, O. (2016). D-sorbitol-induced phase control of TiO_2 nanoparticles and its application for dye-sensitized solar cells. *Sci. Rep.* 6, 20103. doi:10.1038/srep20103

Shi, H., Zhou, Z., Li, W., Fan, Y., Li, Z., and Wei, J. (2021). Hydroxyapatite based materials for bone tissue engineering: A brief and comprehensive introduction. *Crystals* 11, 149–218. doi:10.3390/cryst11020149

Siswanto, S., Hikmawati, D., Kulsum, U., Izak Rudyardjo, D., Apsari, R., and Aminatun, A. (2020). Biocompatibility and osteoconductivity of scaffold porous composite collagen–hydroxyapatite based coral for bone regeneration. *Open Chem.* 18, 584–590. doi:10.1515/chem-2020-0080

Song, Q., Prabakaran, S., Duan, J., Jeyaraj, M., Mickymaray, S., Paramasivam, A., et al. (2021). Enhanced bone tissue regeneration via bioactive electrospun fibrous composite coated titanium orthopedic implant. *Int. J. Pharm.* 607, 120961. doi:10.1016/j.ijpharm.2021.120961

Sulaiman, G. M., Jabir, M. S., and Hameed, A. H. (2018). Nanoscale modification of chrysin for improved of therapeutic efficiency and cytotoxicity. *Artif. Cells, Nanomedicine, Biotechnol.* 46, 708–720. doi:10.1080/21691401.2018.1434661

Sun, H., and Wu, P. (2018). Tuning the functional groups of carbon quantum dots in thin film nanocomposite membranes for nanofiltration. *J. Membr. Sci.* 564, 394–403. doi:10.1016/j.memsci.2018.07.044

Thorpe, C. T., Streeter, I., Pinchbeck, G. L., Goodship, A. E., Clegg, P. D., and Birch, H. L. (2010). Aspartic acid racemization and collagen degradation markers reveal an accumulation of damage in tendon collagen that is enhanced with aging. *J. Biol. Chem.* 285, 15674–15681. doi:10.1074/jbc.m109.077503

Ul Ain, Q., Zhang, H., Yaseen, M., Rasheed, U., Liu, K., Subhan, S., et al. (2020). Facile fabrication of hydroxyapatite-magnetite-bentonite composite for efficient adsorption of Pb(II), Cd(II), and crystal violet from aqueous solution. *J. Clean. Prod.* 247, 119088. doi:10.1016/j.jclepro.2019.119088

You, Z., Zhang, N., Guan, Q., Xing, Y., Bai, F., and Sun, L. (2019). High sorption capacity of U(VI) by COF-based material doping hydroxyapatite microspheres: Kinetic, equilibrium and mechanism investigation. *J. Inorg. Organomet. Polym. Mat.* 30, 1966–1979. doi:10.1007/s10904-019-01420-9

Zeng, W., Yan, Y., Zhang, F., Zhang, C., and Liang, W. (2013). Chrysin promotes osteogenic differentiation via ERK/MAPK activation. *Protein Cell* 4, 539–547. doi:10.1007/s13238-013-3003-3